Disclosing the Annihilation Effect of Ion-implantation Induced Defects in Single-crystal Diamond by Resonant MEMS

Guo Chen [b, a], Zilong Zhang [b], Yasuo Koide [c], Satoshi Koizumi [b],
Zhaohui Huang [a], Meiyong Liao [b, *]

[a] Engineering Research Center of Ministry of Education for Geological Carbon Storage and Low Carbon Utilization of Resources, Beijing Key Laboratory of Materials Utilization of Nonmetallic Minerals and Solid Wastes, National Laboratory of Mineral Materials, School of Materials Science and Technology, China University of Geosciences, Beijing, 100083, China

[b] Ultra-wide Bandgap Semiconductors Group, Research Center for Electronics and Optical Materials, National Institute for Materials Science, Namiki 1-1, Tsukuba, Ibaraki 305-0044, Japan

[c] Next-generation Semiconductors Group, Research Center for Electronics and Optical Materials, National Institute for Materials Science, Namiki 1-1, Tsukuba, Ibaraki 305-0044, Japan

Correspondence: Meiyong Liao* (meiyong.liao@nims.go.jp)

Abstract

Single-crystal diamond presents as an ideal semiconductor material for high-performance and high-reliability MEMS devices, on account of its outstanding mechanical and physical properties. A smart-cut technology based on ion-implantation was proposed to fabricate the SCD-on-SCD MEMS resonators. However, the ion-implantation damage induced defects would degrade the quality (Q) factors of the diamond MEMS resonators. Here, we systematically investigate the effect of ultra-high vacuum annealing on the resonance properties of SCD cantilevers. It is observed that the Q factors are markedly improved by nearly twice after annealing at 1100^{o}C due to the annihilation of the ion implantation induced damage in the resonators. Therefore, reducing the defects in the resonators by high-temperature annealing the as-fabricated SCD MEMS cantilevers is one of the strategies to improve the Q factors. This work also proves out that MEMS represents a more sensitive tool for characterizing the crystalline quality of diamond, compared with the conventional structural methods.

Keywords: Single-crystal diamond, MEMS, Quality factor, High-temperature Annealing,

1. Introduction

Single-crystal diamond (SCD) is an outstanding candidate for high-performance and high-reliability microelectromechanical system (MEMS) devices, due to its exceptional mechanical, physical, chemical, and electronic properties [1-6]. To be specific, compared to other traditional materials, such as Si, SiC and III-nitride, SCD has superior mechanical strength, ultra-wide bandgap, the highest Young's modulus and thermal conductivity, and low coefficient of thermal expansion with excellent chemical inertness [7-10]. Therefore, the quality (Q) factor and reliability of SCD MEMS resonators could be improved greatly, compared with the state-of-the-art resonators prepared by other materials [3, 11, 12]. It has been recognized that the ultra-wide bandgap energy and deep-level nature of existing dopants in diamond provide a significant advantage over other semiconductors for the development of high Q-factor MEMS resonators [13, 14].

We have established a smart-cut method based on the ion-implantation assisted lift-off (IAL) technique to fabricate the SCD-on-SCD MEMS resonators with ultrahigh Q factors over one million with precise controllability and high reproducibility [15-17]. However, ion-implantation can obviously induce damages in a semiconductor crystal, including vacancies and interstitials which significantly affect the electrical, optical, and mechanical properties of the material. The as-fabricated SCD MEMS resonators showed typical Q factors in the level of several thousand [14, 16]. It is understood that the degradation of the Q factors of SCD cantilevers was due to the ion-implantation induced defects [16, 18-19]. There is a need to explore the correlation between ion-implantation-induced defects and the Q factor of diamond MEMS resonators to further improve the performance of MEMS devices. Conventional structural techniques like X-ray diffraction (XRD), transmission electron microscopy (TEM), and Raman spectroscopy face challenges in detecting and observing atomic-scale defects, particularly in single-element semiconductors such as diamond [20-24]. These techniques rely on the scattering or absorption of electromagnetic radiation by the crystal lattice, which is not strongly affected by isolated point defects [25-28]. In the

meanwhile, reducing the defects in the resonators by annealing the as-fabricated SCD MEMS cantilevers in an ultra-high vacuum ambient is one of the strategies to improve the Q factors [17, 29, 30]. Nevertheless, the annealing effect on the SCD MEMS cantilevers is not well understood and has not been systematically investigated yet [15, 31, 32]. We infer that defects could also be detected by a MEMS resonator through measurement of the Q factors.

In this work, we aim to systematically investigate the effect of ultra-high vacuum (UHV) annealing on the resonance properties of the SCD cantilevers and examine the effect of the ion-implantation induced damages in diamond by measuring the Q factors of SCD MEMS cantilevers. The resonance frequency and Q factors were measured and analyzed after annealing the SCD cantilevers from 900°C to 1100°C followed by a hydrogen (H_2) plasma cleaning process. It was found that the Q factors were markedly improved from the typical values around 8,000 to over 15,000 after the annealing treatment at 1100°C. The improvement of the Q factors of the SCD cantilevers is due to the annihilation of the defects induced by ion-implantation, which was detected by MEMS. This work reveals that MEMS is a more sensitive and promising tool for characterizing the crystalline quality and monitoring the defects in diamond, compared to conventional technologies.

2. Experimental

2.1 Fabrication of the SCD MEMS Cantilevers

As shown in Fig. 1 (a), the SCD MEMS cantilevers were fabricated by using a smart-cut method, which employed the ion-implantation assisted lift-off technique started from the SCD epilayer grown on a high-pressure and high-temperature (HPHT) type-Ib (100) SCD substrate. The dimensions of the SCD substrate are around 3 mm × 3 mm × 0.5 mm. Prior to the microwave plasma chemical vapor deposition (MPCVD) growth, a damaged sacrificial graphite-like layer was embedded in the SCD substrate by using high-energy ion implantation to facilitate the release of the resonator structure. Specifically, the substrate was implanted with carbon ions at an energy of 180 keV and

a dose of 10^{16} cm^{-2}. The diamond epilayers were grown by using a methane CH_4/H_2 gas mixture as the reaction precursor, with a 1.5% CH_4 concentration, a hydrogen flow rate of 500 sccm, a chamber pressure of 11 kPa, a microwave power of 1 kW, and a substrate temperature of around 900ºC. The SCD cantilevers were fabricated by using a standard photolithography process, in which an aluminum layer with a thickness of 50 nm was deposited on the patterned SCD homoepitaxial layer, acting as a mask for the forward reactive ion etching (RIE). The RIE parameters for the process were an oxygen (O_2) flow of 90 sccm, a radio frequency (RF) power of 800 W, and a bias power of 20 W, at a pressure of 0.5 Pa. At last, the SCD cantilevers were released by removing both the graphite-like carbon layer and the aluminum film. The as-fabricated SCD cantilevers had an oxygen (O)-terminated surface due to the wet release process. The diamond cantilevers had a thickness (t), width (W), and length (L) of approximately 1 μm, 10-12 μm, and 30-160 μm, respectively. The optical image of the SCD MEMS cantilevers is shown in Fig. 1 (b), which was on a SCD substrate with an epitaxial diamond layer. In Fig. 1 (c), the gradient color on the SCD cantilevers indicates the changes in distance between the upper surface of the cantilever and the substrate, as well as the bending of the SCD cantilevers.

2.2 UHV Annealing and H_2 Plasma Treatment

In order to explore the effect of annealing on the resonance property of SCD cantilevers, the sample was annealed in ultra-high vacuum (UHV) chamber with a base pressure less than 10^{-9} Pa. The temperature for annealing was adjusted to be 900°C, 950°C, 1000°C, 1050°C, and 1100°C for 7 hours at each treatment. The current used varies with the target annealing temperature, which was from 9.0 A to 11.0 A. Fig. 1 (d) illustrates the SCD sample with cantilevers during high-temperature annealing. To examine the surface-termination effect on the Q factors of the SCD cantilever, a H_2 plasma treatment was performed by using the MPCVD after each UHV annealing and resonance measurement, as shown in Fig. 1 (e). Before the H_2 plasma treatment, the chamber was first evacuated to a pressure of approximately 10^{-3} Pa. The H_2 flow rate was 500 sccm and the pressure was 11 kPa. The substrate temperature was controlled

to be around 850°C, less than the temperatures for UHV annealing. The H_2 plasma treatment was conducted after each UHV annealing. The H_2 plasma treatment leads to a hydrogen (H)-termination of the SCD cantilevers surface. Therefore, the surface condition is assumed to be the same for each measurement for the H-terminated SCD cantilever.

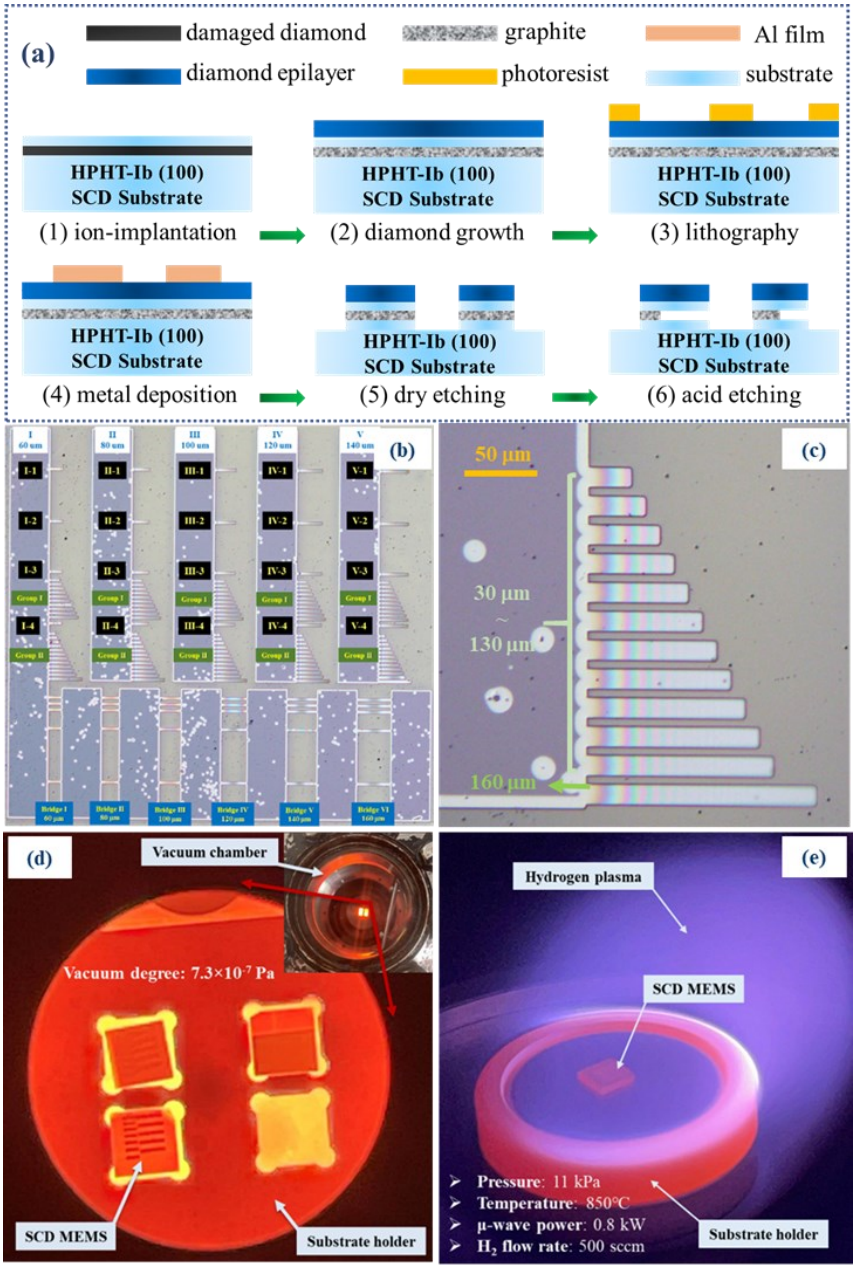

Fig. 1. (a) Fabrication diagram of the SCD MEMS cantilevers. Optical images of (b) the SCD MEMS cantilevers and (c) the enlarged SCD cantilevers with the length from 30 μm to 160 μm. Digital photos of the configuration of the sample during the (d) UHV annealing and (e) H_2 plasma treatment.

2.3 Characterization

In order to investigate the effect of annealing on the resonance property of the SCD cantilevers, the resonance frequency and Q factors of the SCD resonators were measured in a high-vacuum (less than 10^{-5} Pa) chamber at room temperature by using a laser Doppler vibrometer (LDV, LV 1710) system to avoid air/gas damping. The sample was set onto the piezoceramic actuator directly. The actuation of the diamond cantilevers was achieved using a piezoceramic element that was actuated by applying a radio-frequency voltage signal. This allowed for the actuation of the cantilevers while avoiding nonlinearity of the resonance. By fitting the resonance spectra to a Lorentz function, the resonance frequency and Q factors were obtained. The mechanical resonance properties of the SCD cantilevers were investigated for each UHV annealing and H_2 plasma treatment. The UHV annealing and resonance properties were performed in different vacuum chambers. However, from the H-terminated SCD cantilever, it was confirmed the Q factor variation due to air exposure is negligible compared to UHV annealing. Since after each UHV annealing, a hydrogenation process of the SCD cantilevers was adopted, the surface condition is thus assumed to be similar. This exclude the effect of the surface effect on the Q factor improvement after each UHV annealing. The geometric profiles of the SCD cantilevers were measured by a Keyence 3D laser scanning microscope. A 3D Raman spectroscopy (WITec α-300R) was used to measure the SCD epilayer and substrate. The instrument utilized a laser with a wavelength of 532 nm and a power of 20 mW. All measurements were performed in the backscattering geometry at room temperature. The wave-number of the peak position was calibrated by using a high-quality type-IIa diamond, resulting in a value of 1332.4 cm^{-1} for the first-order diamond line.

3. Results and Discussion

3.1 Dependence of Resonance Property on Annealing

In this work, we mainly investigated the effects of UHV annealing on the resonance properties of the SCD MEMS cantilevers. Fig. 2 (a) is typical resonance

frequency spectra of a SCD cantilever with a length of 120 μm, width of 10 μm and thickness of ~1 μm, which shows a Lorentz shape. The Q factor and resonance frequency of the cantilever were determined from the frequency resonance spectrum by fitting it to the Lorentz function. The Q factor is calculated as the Formula (1) [14].

$$Q = f/\Delta f \quad (1)$$

Specifically, the Q factor is obtained by dividing the resonance frequency (f) by the full-width at half-maximum (Δf) of the resonance peak. The amplitude of the resonance increases in a linear manner as the amplitude of the driving radio-frequency (RF) signal for the cantilevers is increased. As displayed in Fig. 2 (b), despite the annealing and surface terminations, the resonance frequency of the SCD cantilevers follows the inverse power law relationship with the length of the cantilevers, revealing the excellent controllability and reliability of the SCD-on-SCD MEMS structures, as well as the uniformity of the cantilevers in thickness.

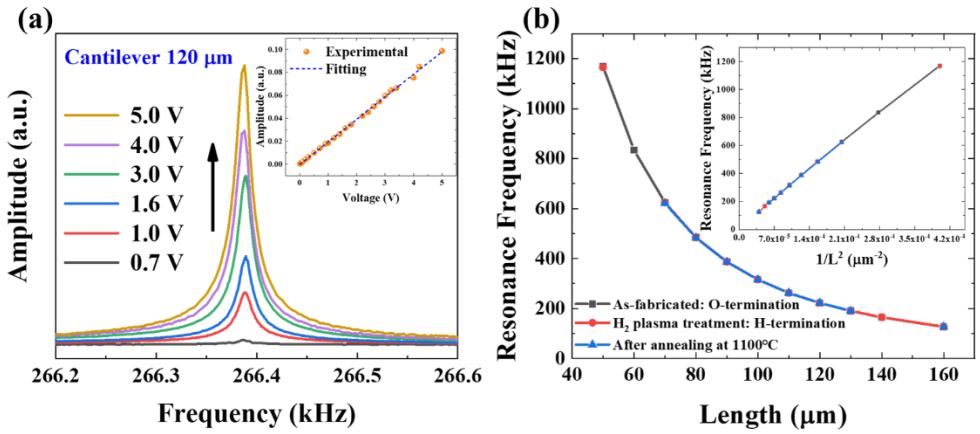

Fig. 2. (a) Typical frequency spectra obtained with different RF amplitude applied to the piezoceramics in the range of 0.7 to 5.0 V. The inset showing a linear relationship between the resonance amplitude and the actuation voltage applied to the piezoceramics. (b) Dependence of the resonance frequency on different cantilever lengths after annealing and the H_2 plasma treatment. The inset showing the resonance frequency follows the inverse power law relationship well with the length.

The frequency variations of the SCD cantilevers with the annealing temperature and H_2 plasma treatment are also investigated by comparing with those of the as-fabricated ones, as shown in Fig. 3. The hydrogenation process is just to ensure the same surface condition of the SCD cantilever and to differ from the bulk effect on the Q factor. As an example, the data of the SCD cantilevers with length of 100 μm, 110 μm, 120 μm and 130 μm is presented. In Fig. 4, the dependence of the ratio of the resonance frequency change δf/f for different cantilever lengths after each annealing process is shown. Note that the resonance frequency change of the SCD cantilevers here refers to the resonance frequency just after the former annealing. The fluctuation of the resonance frequency is generally small with the UHV annealing process. The reason for the abnormal change for the cantilevers with length exceeding 120 μm is not clear, likely due to surface stress or uncertain contaminations. Therefore, all in all, it can be deduced that annealing has little influence on the resonance frequency.

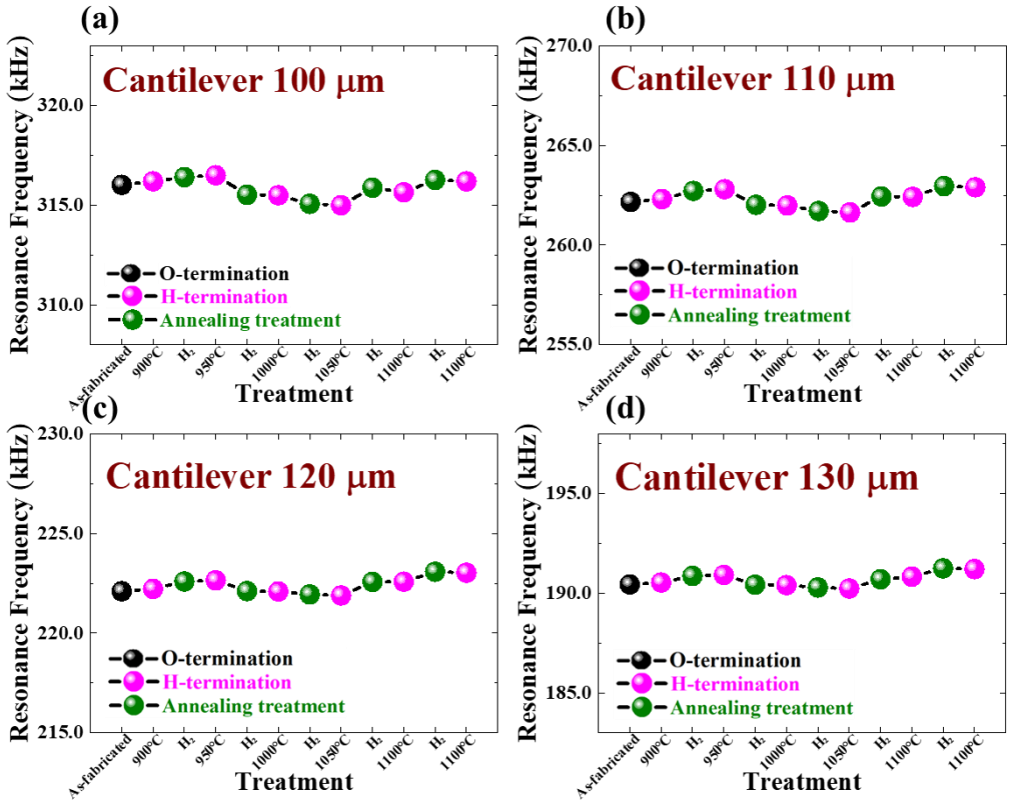

Fig. 3. The resonance frequency changes with H_2 plasma treatment and different annealing temperature of the SCD cantilevers with a length of (a) 100 μm, (b) 110 μm, (c) 120 μm and (d) 130 μm.

Quality factor is one of the most important parameters for MEMS cantilevers [33, 34], which determines the MEMS devices properties, such as the sensitivity, resolution, respond speed, and noise level for MEMS resonant sensors. On the other hand, the Q factors are intrinsically affected by the crystal imperfections such as point defects and dislocations. By annealing the SCD cantilevers at different temperatures up to 1100°C, the Q factors were improved greatly. As the Formula (2) shows, for the cantilever, the Q factors of the cantilever are determined by a sum of various kinds of energy dissipations, such as the clamping dissipation, surface dissipation, thermoelastic dissipation, defects dissipation and other dissipations [14].

$$Q_{Total}^{-1} = Q_{Clamp}^{-1} + Q_{Surface}^{-1} + Q_{TED}^{-1} + Q_{Defect}^{-1} + Q_{Other}^{-1} \quad (2)$$

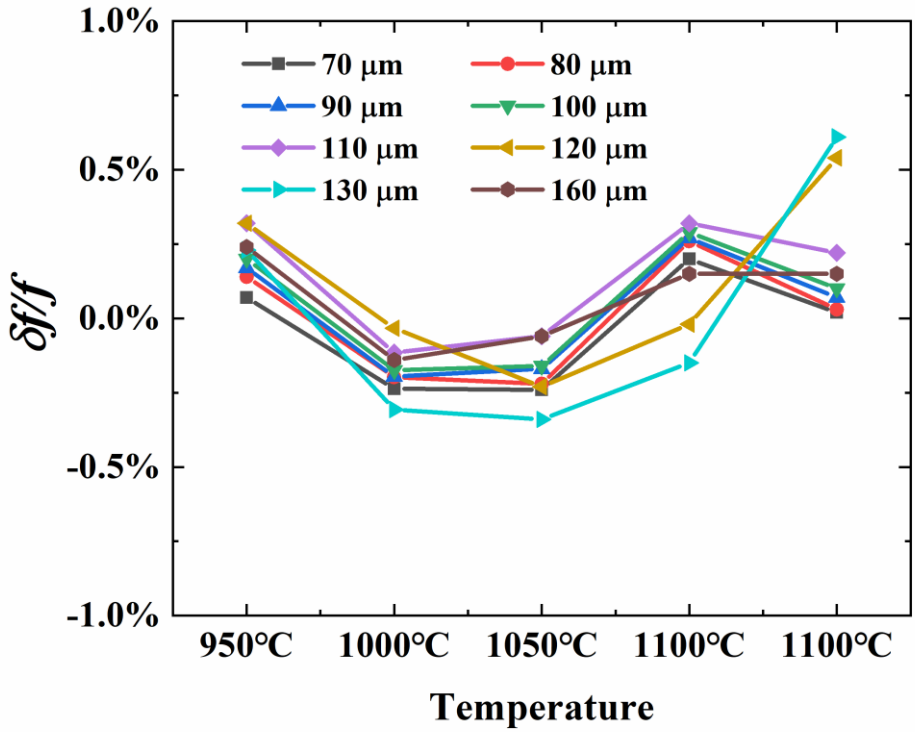

Fig. 4. The dependence of *δf/f* on the annealing temperature for the cantilever with different lengths.

In Fig. 5 (a), the relationship between the Q factors and the length of different SCD cantilevers is depicted. It can be observed that the Q factor increases with the length of the cantilever increasing due to clamping loss. As the cantilever length

increases, the clamping loss reduces, leading to a higher Q factor. However, when the cantilever length beyond 120 μm, the Q factor no longer increases significantly with further increases in cantilever length. The bulk defects and surface effect dissipation are considered here as the dominant mechanisms. Bulk defects within the SCD cantilever can introduce additional sources of energy dissipation, reducing the overall Q factor. The surface effects, such as adsorbates, can also contribute to dissipation, but can be distinguished by H-termination of the SCD cantilever from the UHV annealing. Fig. 5 (b) shows the Q factors are markedly improved from the typical values around 8,000 to over 15,000 after the annealing treatment at 1100°C for 7 hours. The enhancement of the Q factors with annealing is due to the annihilation of the defects in the SCD cantilevers, therefore, reducing the defects induced energy loss. The relationship of the Q factor of the SCD cantilever with other different lengths and annealing temperature are depicted in Fig. S1, revealing the similar tendency.

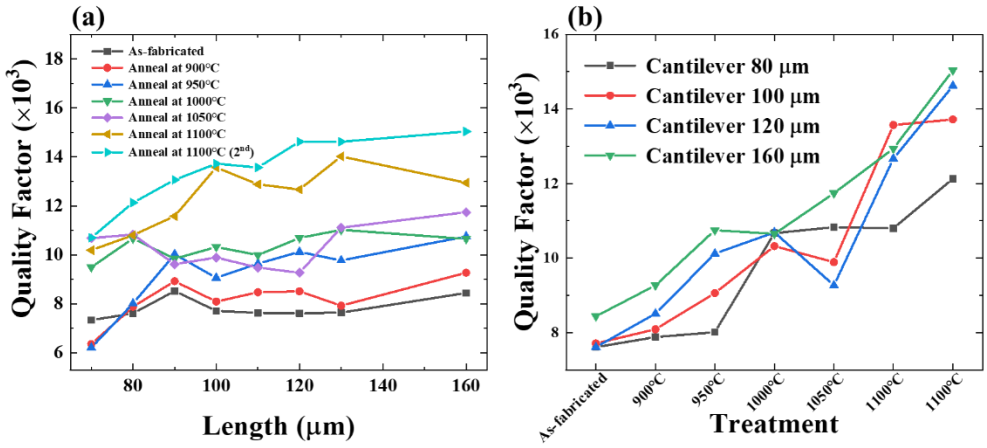

Fig. 5. (a) Dependence of the Q factors on the length of different SCD cantilevers. (b) The variations of the Q factors with different annealing temperatures of the SCD cantilevers with different lengths.

As shown in Fig. 6, the Q factors increase after each annealing above 900°C, indicating that this temperature can either reduce or eliminate the defects to some extent. The consistent dips in Q factor observed for all cantilevers at 1050°C possibly are attributed to the uncertain surface contamination. And a subsequent H_2 plasma treatment followed the annealing increases the Q factors further. The increase of the Q

factors by the H_2 plasma treatment is likely due to the surface cleaning, which reduces the surface energy dissipation. We also investigated the O-termination effect on the Q factors of the SCD cantilever in a boiling H_2SO_4 solution. To exclude the surface effect on the marked improvement of the Q factor, the SCD cantilevers were oxidized again after the H_2 plasma treatment followed the high-temperature annealing. Although there is increase in the Q factors by H-termination or O-termination, the increased amplitude is much less than the annealing effect. The experimental observation is reproduced for most of the SCD cantilevers despite the length variation. The H-termination thus excludes the effect of the surface effect on the Q factor improvement after each UHV annealing.

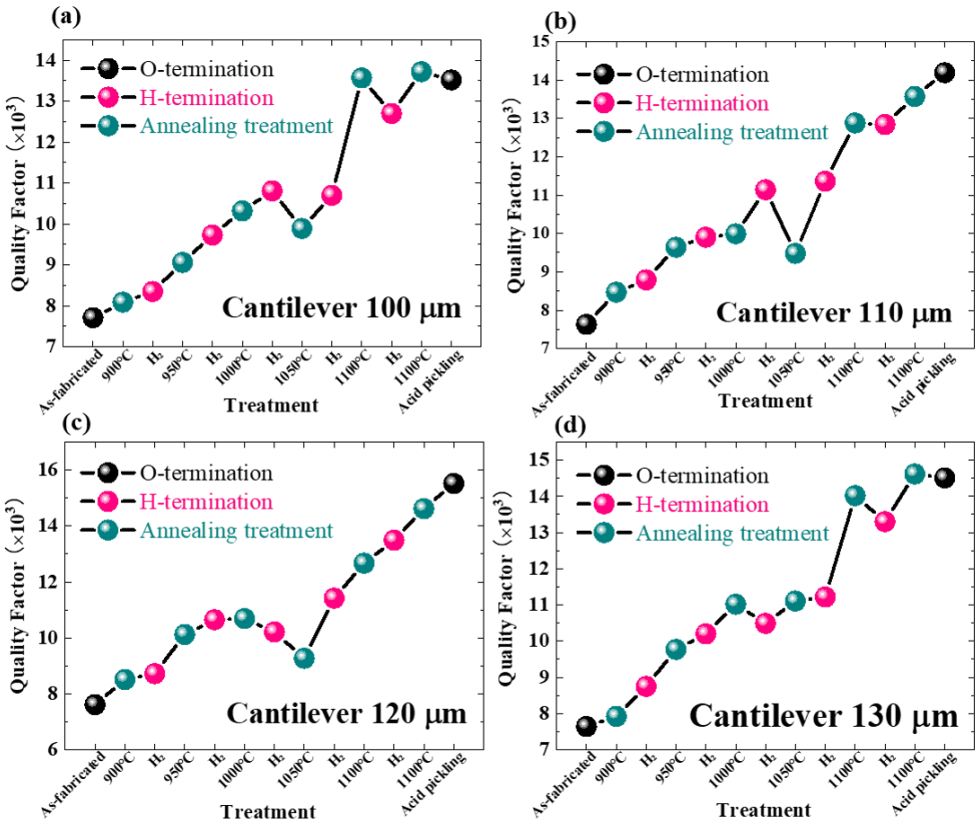

Fig. 6. Q factor changes with the H_2 plasma treatment and different annealing temperature of the cantilevers with a length of (a) 100 μm, (b) 110 μm, (c) 120 μm, and (d) 130 μm.

The statistical analysis of the Q factors of the SCD cantilever are conducted. A total of 114 cantilevers were subjected to quantitative analysis after annealing, as indicated in Table 1. The formula $\Delta Q = Q_H - Q_L$ represents the calculation for the change in Q factor (ΔQ) after two annealing temperature: Q_H refers to the Q factor value in the higher annealing temperature, while Q_L represents the Q factor value in the lower annealing temperature. More than 70% cantilevers show the increase of the Q factor after each annealing. As shown in Fig. 7, an activation energy around 0.28 eV was obtained by plotting ln Q as a function of the annealing temperature, which is [35-37]

$$Q = \exp(-E_a/kT) \quad (3)$$

where E_a is the thermal activation energy, and T is the annealing temperature. The activation energy refers specifically to the energy required for the annihilation of the defects induced by annealing.

Table 1. Quantitative analysis of the Q factor changes for 114 cantilevers after annealing.

Different Treatment		**$\Delta Q = Q_H - Q_L$**	
		Increased	**Decreased**
Anneal only	900ºC - 950ºC	94.44%	5.56%
	950ºC - 1000ºC	70.37%	29.63%
	1000ºC - 1050ºC	74.51%	25.49%
	1050ºC - 1100ºC	84.95%	15.05%
	1100ºC - 1100ºC	85.06%	14.94%
H_2 Plasma only	900ºC - 950ºC	84.11%	15.89%
	950ºC - 1000ºC	71.57%	28.43%
	1000ºC - 1050ºC	73.68%	26.32%
	1050ºC - 1100ºC	94.44%	5.56%
	1100ºC - 1100ºC	88.37%	11.63%

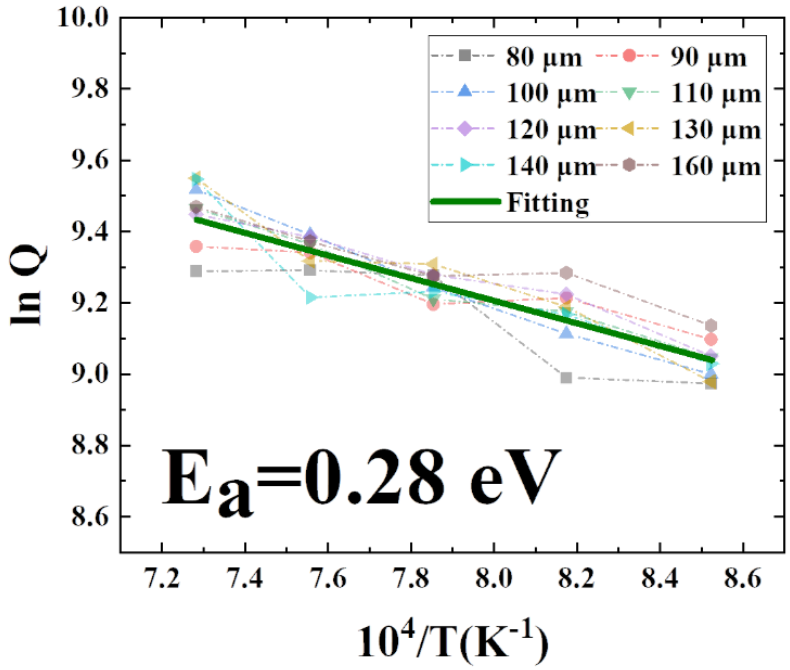

Fig. 7. Arrhenius plot of the ln Q as a function of annealing temperature. The slope gives an activation energy of E_a = 0.28 eV.

3.2 Analysis of the Surface Stress

The bending profile of radius and surface stress after each annealing were analyzed by the 3D laser microscope. Fig. 8 shows the 3D geometrical profile images of the SCD cantilevers after annealing at different temperatures, which clearly show an upward bending attributed to the presence of residual stress. ΔH here means the upward bending amplitude of the end of the SCD cantilever referring to the supporting junction of the cantilever. The origin of the surface stress observed here can be ascribed to surface imperfections, surface reconstruction, and the presence of absorbates during the fabrication process [38]. Fig. 9 displays the height profile of the SCD cantilever with different length after annealing at 1100ºC and the SCD cantilever with the same length at 140 μm after annealing from 900ºC to 1100ºC. As is shown, the upward bending increased with the length of the cantilever. But, for the same cantilever, such as the 140-μm length one, the upward bending is nearly the same under different annealing temperatures, which is around 5 μm. Therefore, it seems that the annealing changes little about the surface stress.

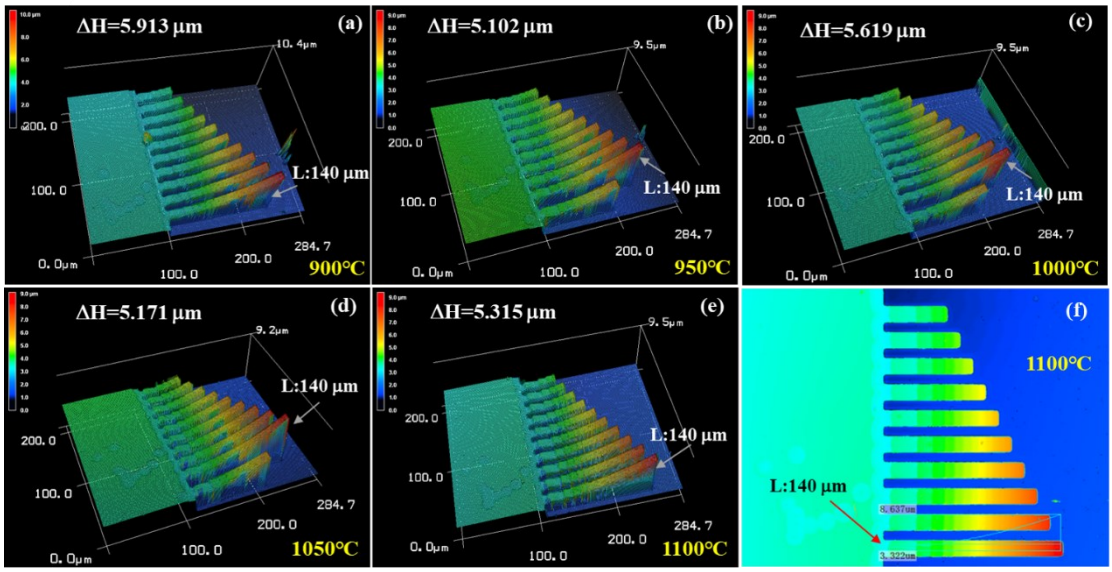

Fig. 8. The 3D profile images of the SCD cantilevers after annealing at different temperatures: (a) 900°C, (b) 950°C, (c) 1000°C, (d) 1050°C, and (e ~ f) 1100°C.

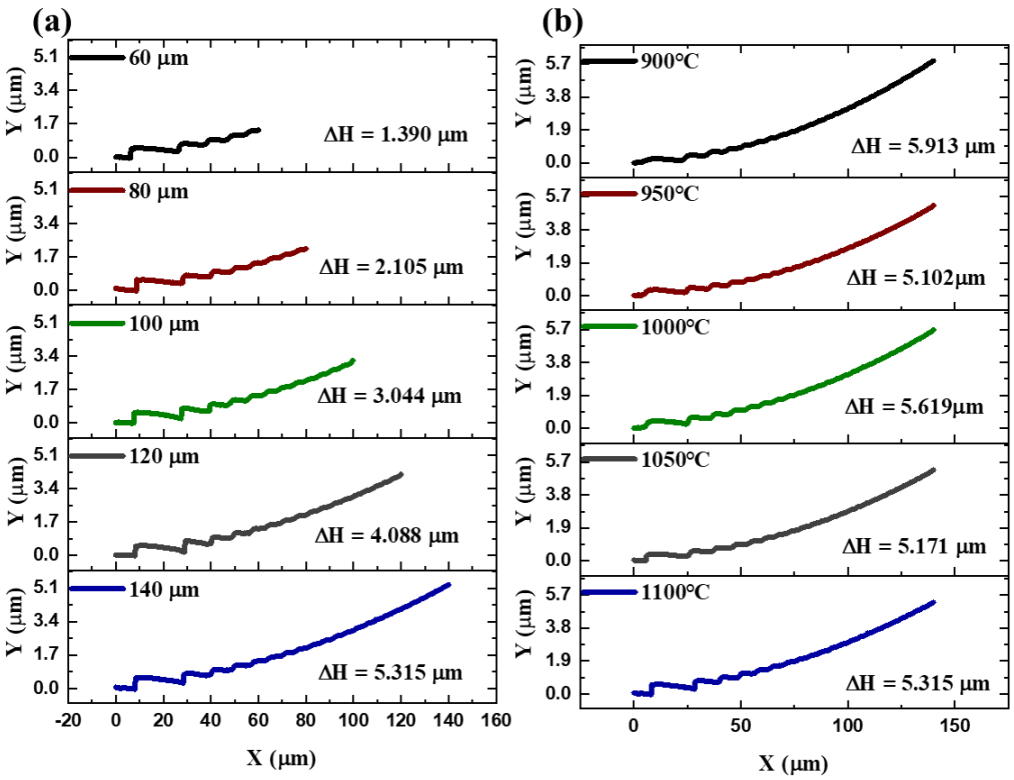

Fig. 9. The height profile of (a) the SCD cantilever with different length after annealing at 1100°C and (b) the SCD cantilever with the same length (140 μm) after annealing at different temperature from 900°C to 1100°C.

The modified Stoney equation allows for the calculation of the surface stress difference Δδ between the top and bottom surfaces of the cantilevers by

$$\Delta\sigma = Et_{Cant}^2\big(6R(1-v)\big)^{-1} \quad (4)$$

where R, ν, E, and t_{Cant} represent the radius of the curvature, the Possion ratio, the Young's modulus of the cantilever, and thickness of the cantilever respectively [39-41]. Table 2 shows the calculated surface stress (Δδ) of the cantilevers under different annealing temperatures. According to the modified Stoney equation, the surface stress can be calculated to range from 126 N/m to 225 N/m. The surface stress decreases with the length of the cantilever, which can be also observed from Fig. 10, showing the dependence of the curvature k, which equals to 1/R, and surface stress Δδ on the cantilever length. The reason of the stress variation with length is not clear, possibly due to the estimation method by Stoney equation, without considering the anisotropic elastic response of diamond. But for the same cantilever, the surface stress only decreases markedly after the first annealing. Although MEMS technology is capable of analyzing the stress and detecting the changes, its high sensitivity to various external factors makes it difficult to distinguish the true origin at this moment. Even minor changes in stress can alter the frequency of the cantilever. While measuring stress changes due to annealing alone is possible, the influence of external environmental factors, such as adsorption, temperature, and humidity changes, can also contribute to stress and complicate identifying the source of stress.

Table 2. The surface stress Δδ of the SCD cantilevers after annealing at different temperature (N/m)

Length	As-fabricated	900°C	950°C	1000°C	1050°C	1100°C
60 μm	225	160	126	163	152	168
80 μm	216	157	128	150	138	154
100 μm	207	157	128	147	142	148
120 μm	202	156	128	146	136	141
140 μm	198	153	132	145	134	138

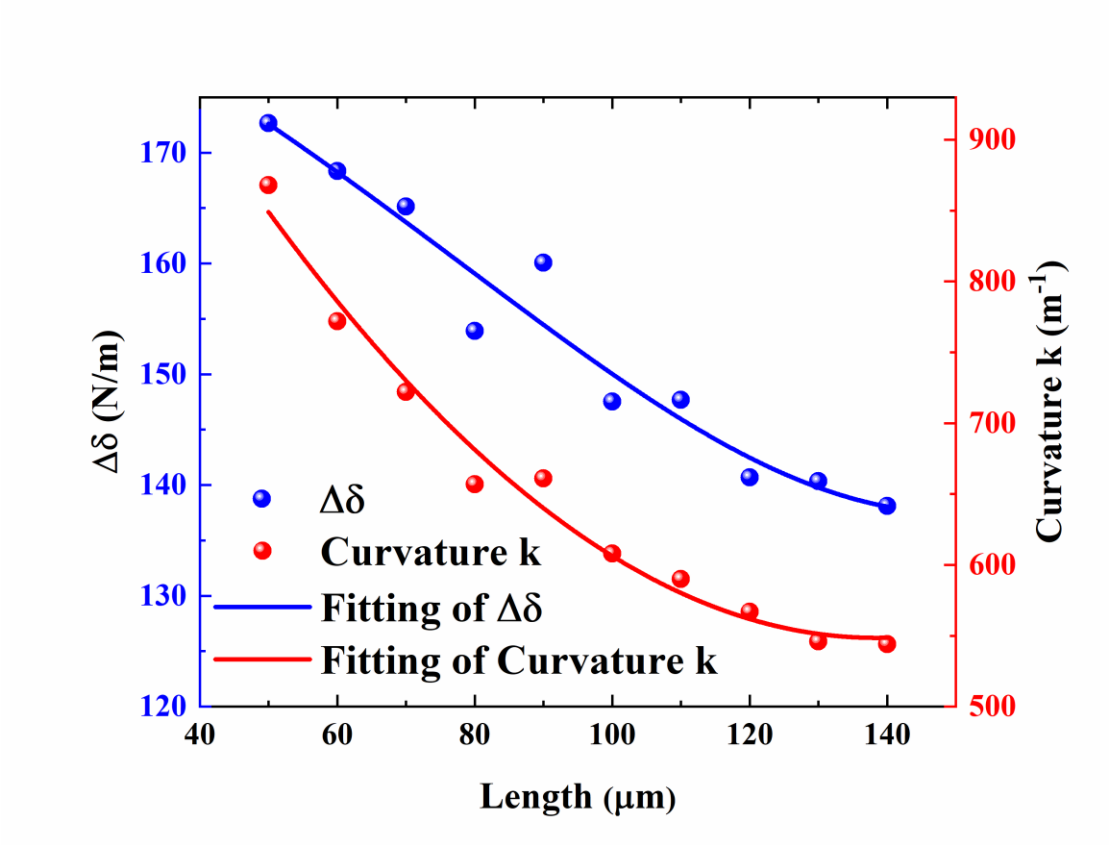

Fig. 10. The relationship among the curvature k, surface stress Δδ, and SCD cantilever length.

3.3 Raman Characterization of the SCD MEMS Resonators

As discussed, the crystal imperfection strongly affects the Q factor of the SCD cantilevers. We tried to use Raman spectroscopy to investigate the annihilation effect of the defects that affect the Q factors of the SCD cantilevers. We performed Raman

measurements at the MPCVD SCD epilayer location in the same sample that the graphite-like carbon is not removed. The SCD substrate effect on the Raman spectra is thus nearly excluded and the signal is nearly from the CVD epilayer above the graphite-like layer.

Fig. 11 displays the Raman spectra and statistic distribution of the full-width at half-maximum (FWHM) and Raman shifts in the area of the SCD epilayer on the graphite-like layer. We present here the Raman data of the as-grown diamond epilayer and the one annealed at 1100ºC (For other annealing temperatures, see Fig. S2 in Supplementary data). Table 3 lists the statistic Raman shifts and FWHM values, as well as the calculated surface stress, of the epilayer and substrate at different annealing temperatures. The surface stress is calculated by using the following equation [36],

$$\delta(GPa) = -0.625\Delta\omega\,(cm^{-1}) \quad (\Delta\omega = \omega_1 - \omega_0,\ \omega_0 = 1332.4cm^{-1}) \qquad (5)$$

where ω_0 means the Raman shift in the unstrained crystal, ω_1 means the detected Raman shift. As indicated, the surface stress obtained from the difference of Raman shift between the epilayer and type-Ib diamond exhibits a negligible disparity. These Raman shift and FWHM values were obtained by fitting a Gaussian function to the statistical distribution of the Raman shift and FWHM for both the epilayer and substrate after annealing. Raman spectra of the epilayer was observed to be centered at around 1332.5 cm^{-1} with varying annealing treatment. The FWHM of the SCD epilayer is around 1.8 cm^{-1}, which keeps nearly unchanged upon the annealing. Therefore, Raman spectra could not distinguish the annealing effect on the improvement of the crystal quality or the annihilation of the ion-implantation induced damages.

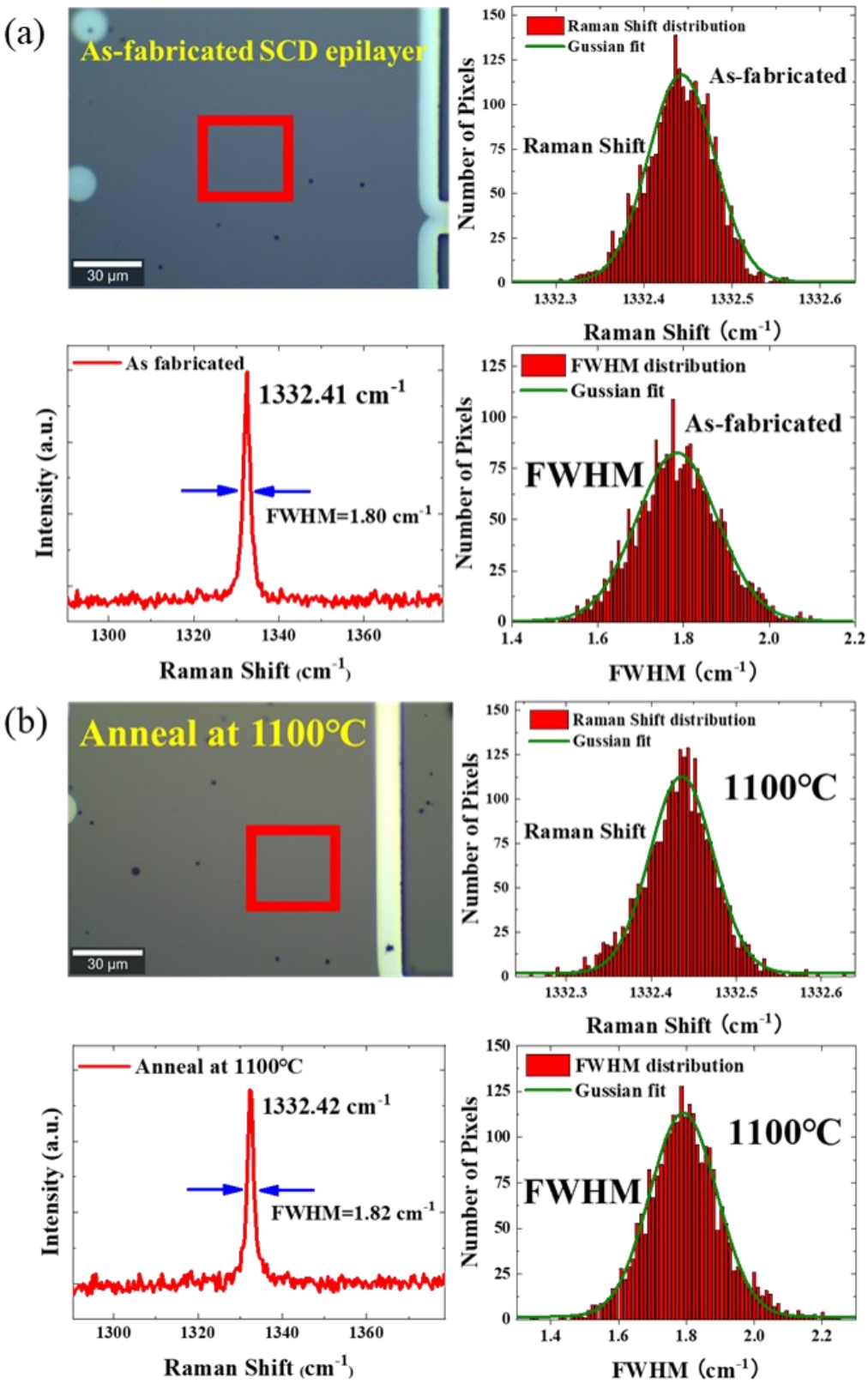

Fig. 11. The video images, Raman spectra, and statistic distribution of the Raman shift and FWHM of the (a) as-fabricated SCD epilayer and (b) the one after annealing at 1100°C.

Table 3. Statistics of the Raman shift and FWHM of the SCD epilayer and substrate after different annealing temperature.

Annealing	Raman shift (cm^{-1})	FWHM (cm^{-1})		Surface Stress
	Epilayer	Epilayer	Substrate	δ (MPa)
As-fabricated	1332.41	1.80	2.06	54.69
900°C	1332.43	1.78	2.07	46.75
950°C	1332.46	1.80	2.03	27.50
1000°C	1332.43	1.69	1.96	42.81
1050°C	1332.45	1.72	1.99	31.81
1100°C	1332.42	1.82	2.04	50.69

The change of the Raman shifts or surface stress is very small after annealing. Nevertheless, in terms of the Q factors results, annealing has great influence on the diamond quality, based on the marked increase of the Q factors. Therefore, the Q factors of the SCD cantilever is more sensitive for characterizing the crystalline quality and monitoring the defects in diamond.

4. Conclusions

In conclusion, the effect of ultra-high vacuum annealing on the resonance properties of the SCD MEMS cantilevers was systematically investigated. The resonance frequency and Q factors were measured and analyzed after annealing. Even after annealing, the resonance frequency of the SCD cantilevers consistently followed an inverse power law relationship with the length of different SCD MEMS cantilevers, highlighting the exceptional reliability of SCD MEMS. It was found that the Q factors were markedly improved after the annealing from 900°C to 1100°C, eventually increased from the typical values around 8,000 to over 15,000 at 1100°C. The improvement of the Q factors is due to the annihilation of the defects within the SCD cantilevers. The surface effect on the Q factors of the SCD MEMS cantilevers was much less compared to the UHV high-temperature annealing. The annihilation of the

ion-implantation induced lattice damages in the SCD cantilevers were disclosed by measuring the Q factor of the resonators. It is revealed that MEMS may represent a more sensitive tool for characterizing crystalline quality compared with the conventional structural methods.

Acknowledgements

This work was partially supported by a JSPS KAKENHI (Grant Number 20H02212, 22K18957, 15H03999), Grant-in-Aid for JSPS Research Fellows (22F21341), Bilateral joint research between JSPS/CAS and Nanotechnology Platform projects sponsored by the Ministry of Education, Culture, Sports, and Technology (MEXT) of Japan. Guo Chen also gratefully thanked financial support from China Scholarship Council (No. 202006400023).

Declaration of Competing Interest

The authors declare that they have no known competing financial interests or personal relationships that could have appeared to influence the work reported in this paper.

References

[1] H. Wu, Z. Zhang, L. Sang, T. Li, J. You, M. Imura, Y. Koide, M. Liao, Precise characterization of atomic-scale corrosion of single crystal diamond in H2 plasma based on MEMS/NEMS, Corrosion Science 170 (2020).

[2] Z. Zhang, L. Sang, J. Huang, L. Wang, Y. Koide, S. Koizumi, M. Liao, Enhancement of magnetic sensing performance of diamond resonators coupling with magnetic-strictive FeGa films by various interlayers, Carbon 200 (2022) 401-409.

[3] P. Ovartchaiyapong, L. Pascal, B. Myers, P. Lauria, A. Bleszynski Jayich, High quality factor single-crystal diamond mechanical resonators, Applied Physics Letters 101(16) (2012) 163505.

[4] M. Liao, Y. Koide, Carbon-based materials: growth, properties, MEMS/NEMS technologies, and MEM/NEM switches, Critical Reviews in Solid State and Materials Sciences 36(2) (2011) 66-101.

[5] O. Auciello, Science and technology of a transformational multifunctional ultrananocrystalline diamond (UNCDTM) coating, Functional Diamond 2(1) (2022) 1-24.

[6] S. Mi, M. Kiss, T. Graziosi, N. Quack, Integrated photonic devices in single crystal diamond, Journal of Physics: Photonics 2(4) (2020).

[7] Y. Chen, L. Sang, S. Koizumi, Y. Koide, X. Liu, M. Liao, Effect of gas pressure on the quality-factor of single-crystal diamond micro cantilevers, Diamond and Related Materials 129 (2022).

[8] Z. Zhang, Y. Wu, L. Sang, H. Wu, J. Huang, L. Wang, Y. Takahashi, R. Li, S. Koizumi, M. Toda, Coupling of magneto-strictive FeGa film with single-crystal diamond MEMS resonator for high-reliability magnetic sensing at high temperatures, Materials Research Letters 8(5) (2020) 180-186.

[9] G. Zhang, R. Zulkharnay, X. Ke, M. Liao, L. Liu, Y. Guo, Y. Li, H.G. Rubahn, V.V. Moshchalkov, P.W. May, Unconventional giant “magnetoresistance” in bosonic semiconducting diamond nanorings, Advanced Materials (2023) 2211129.

[10] Z. Zhang, W. Zhao, G. Chen, M. Toda, S. Koizumi, Y. Koide, M. Liao, On-chip Diamond MEMS Magnetic Sensing through Multifunctionalized Magnetostrictive Thin Film, Advanced Functional Materials (2023).

[11] Z. Zhang, H. Wu, L. Sang, J. Huang, Y. Takahashi, L. Wang, M. Imura, S. Koizumi, Y. Koide, M. Liao, Single-crystal diamond microelectromechanical resonator integrated with a magneto-strictive galfenol film for magnetic sensing, Carbon 152 (2019) 788-795.

[12] X. Shen, K. Wu, H. Sun, L. Sang, Z. Huang, M. Imura, Y. Koide, S. Koizumi, M. Liao, Temperature dependence of Young's modulus of single-crystal diamond determined by dynamic resonance, Diamond and Related Materials 116 (2021) 108403.

[13] M. Liao, L. Sang, T. Teraji, S. Koizumi, Y. Koide, Ultrahigh Performance On-Chip Single Crystal Diamond NEMS/MEMS with Electrically Tailored Self-Sensing Enhancing Actuation, Advanced Materials Technologies 4(2) (2019) 1800325.

[14] H. Sun, L. Sang, H. Wu, Z. Zhang, T. Teraji, T.-F. Li, J. You, M. Toda, S. Koizumi, M. Liao, Effect of deep-defects excitation on mechanical energy dissipation of single-crystal diamond, Physical review letters 125(20) (2020) 206802.

[15] M. Liao, S. Hishita, E. Watanabe, S. Koizumi, Y. Koide, Suspended single-crystal diamond nanowires for high-performance nanoelectromechanical switches, Advanced Materials 22(47) (2010) 5393-5397.

[16] H. Wu, L. Sang, Y. Li, T. Teraji, T. Li, M. Imura, J. You, Y. Koide, M. Toda, M. Liao, Reducing intrinsic energy dissipation in diamond-on-diamond mechanical

resonators toward one million quality factor, Physical Review Materials 2(9) (2018) 090601.

[17] M. Liao, M. Toda, L. Sang, T. Teraji, M. Imura, Y. Koide, Improvement of the quality factor of single crystal diamond mechanical resonators, Japanese Journal of Applied Physics 56(2) (2017) 024101.

[18] M. Liao, M. Toda, L. Sang, S. Hishita, S. Tanaka, Y. Koide, Energy dissipation in micron- and submicron-thick single crystal diamond mechanical resonators, Applied Physics Letters 105(25) (2014).

[19] Z. Zhang, G. Chen, K. Gu, S. Koizumi, M. Liao, Effect of defects on Q factors of single-crystal diamond MEMS resonators, Functional Diamond 3(1) (2023).

[20] R. Kalish, Ion-implantation in diamond and diamond films: doping, damage effects and their applications, Applied surface science 117 (1997) 558-569.

[21] J. Orwa, K. Nugent, D. Jamieson, S. Prawer, Raman investigation of damage caused by deep ion implantation in diamond, Physical Review B 62(9) (2000) 5461.

[22] A. Crisci, F. Baillet, M. Mermoux, G. Bogdan, M. Nesladek, K. Haenen, Residual strain around grown-in defects in CVD diamond single crystals: A 2D and 3D Raman imaging study, Physica Status Solidi a-Applications and Materials Science 208(9) (2011) 2038-2044.

[23] K. Ichikawa, S. Koizumi, T. Teraji, Propagation of dislocations in diamond (111) homoepitaxial layer, Journal of Applied Physics 132(2) (2022).

[24] K. Ichikawa, T. Shimaoka, Y. Kato, S. Koizumi, T. Teraji, Dislocations in chemical vapor deposition diamond layer detected by confocal Raman imaging, Journal of Applied Physics 128(15) (2020).

[25] F. Bosia, N. Argiolas, M. Bazzan, P. Olivero, F. Picollo, A. Sordini, M. Vannoni, E. Vittone, Modification of the structure of diamond with MeV ion implantation, Diamond and related materials 20(5-6) (2011) 774-778.

[26] E. Nshingabigwi, T. Derry, S. Naidoo, J. Neethling, E. Olivier, J. O'Connell, C. Levitt, Electron microscopy profiling of ion implantation damage in diamond: Dependence on fluence and annealing, Diamond and related materials 49 (2014) 1-8.

[27] S.M. Londoño-Restrepo, L.F. Zubieta-Otero, R. Jeronimo-Cruz, M.A. Mondragon, M.E. Rodriguez-García, Effect of the crystal size on the infrared and Raman spectra of bio hydroxyapatite of human, bovine, and porcine bones, Journal of Raman Spectroscopy 50(8) (2019) 1120-1129.

[28] S. Potgieter-Vermaak, N. Maledi, N. Wagner, J. Van Heerden, R. Van Grieken, J. Potgieter, Raman spectroscopy for the analysis of coal: a review, Journal of Raman Spectroscopy 42(2) (2011) 123-129.

[29] M. Liao, Progress in semiconductor diamond photodetectors and MEMS sensors, Functional Diamond 1(1) (2021) 29-46.

[30] H. Wu, L. Sang, T. Teraji, T. Li, K. Wu, M. Imura, J. You, Y. Koide, M. Liao, Reducing energy dissipation and surface effect of diamond nanoelectromechanical resonators by annealing in oxygen ambient, Carbon 124 (2017) 281-287.

[31] Y. Tao, J.M. Boss, B.A. Moores, C.L. Degen, Single-crystal diamond nanomechanical resonators with quality factors exceeding one million, Nat Commun 5 (2014) 3638.

[32] G. Davies, S.C. Lawson, A.T. Collins, A. Mainwood, S.J. Sharp, Vacancy-related centers in diamond, Phys Rev B Condens Matter 46(20) (1992) 13157-13170.

[33] L. Wei, X. Kuai, Y. Bao, J. Wei, L. Yang, P. Song, M. Zhang, F. Yang, X. Wang, The recent progress of MEMS/NEMS resonators, Micromachines 12(6) (2021) 724.

[34] M.H.M. Najar, Design and Analysis of High Quality Factor Chemical Vapor Deposition (CVD) Diamond Micromechanical Resonators, University of California, Davis2014.

[35] J.S. Aldridge, A.N. Cleland, Noise-enabled precision measurements of a duffing nanomechanical resonator, Physical Review Letters 94(15) (2005).

[36] M. Liao, Y. Koide, J. Alvarez, M. Imura, J.-P. Kleider, Persistent positive and transient absolute negative photoconductivity observed in diamond photodetectors, Physical Review B 78(4) (2008).

[37] D.R. Hang, Y.F. Chen, F.F. Fang, W.I. Wang, Positive and negative persistent photoconductivity in a two-side-doped In0.53Ga0.47As/In0.52Al0.48As quantum well, Physical Review B 60(19) (1999) 13318-13321.

[38] X. Shen, Z. Lv, K. Ichikawa, H. Sun, L. Sang, Z. Huang, Y. Koide, S. Koizumi, M. Liao, Stress effect on the resonance properties of single-crystal diamond cantilever resonators for microscopy applications, Ultramicroscopy 234 (2022) 113464.

[39] K.-S. Chen, K.-S. Ou, Modification of curvature-based thin-film residual stress measurement for MEMS applications, Journal of Micromechanics and Microengineering 12(6) (2002) 917.

[40] G.G. Stoney, The tension of metallic films deposited by electrolysis, Proceedings of the Royal Society of London. Series A, Containing Papers of a Mathematical and Physical Character 82(553) (1909) 172-175.

[41] F. Battiston, J.-P. Ramseyer, H. Lang, M. Baller, C. Gerber, J. Gimzewski, E. Meyer, H.-J. Güntherodt, A chemical sensor based on a microfabricated cantilever array with

simultaneous resonance-frequency and bending readout, Sensors and Actuators B: Chemical 77(1-2) (2001) 122-131.